Inorganic Chemistry

Article

pubs.acs.org/IC

Dense Si_xGe_{1-x} ($0 < x < 1$) Materials Landscape Using Extreme Conditions and Precession Electron Diffraction

George Serghiou,*[,†] Gang Ji,[‡] Monika Koch-Müller,[§] Nicholas Odling,[∥] Hans J. Reichmann,[§] Jonathan P. Wright,[⊥] and Paul Johnson[†,#]

[†]School of Engineering and Centre for Materials Science, University of Edinburgh, Kings Buildings, Mayfield Road, EH9 3JL Edinburgh, U.K.

[‡]Unité Matériaux et Transformations, UMR CNRS 8207, Université Lille 1, 59655 Villeneuve d'Ascq, France

[§]Helmholtz Centre Potsdam, German Research Centre for Geosciences, Telegrafenberg, 14473 Potsdam, Germany

[∥]School of Geosciences, The Grant Institute, University of Edinburgh, Kings Buildings, West Mains Road, EH9 3JW Edinburgh, U.K.

[⊥]European Synchrotron Radiation Facility, F-38043 Grenoble, France

ABSTRACT: High-pressure and -temperature experiments on Ge and Si mixtures to 17 GPa and 1500 K allow us to obtain extended Ge−Si solid solutions with cubic ($Ia\bar{3}$) and tetragonal ($P4_32_12$) crystal symmetries at ambient pressure. The cubic modification can be obtained with up to 77 atom % Ge and the tetragonal modification for Ge concentrations above that. Together with Hume−Rothery criteria, melting point convergence is employed here as a favored attribute for solid solution formation. These compositionally tunable alloys are of growing interest for advanced transport and optoelectronic applications. Furthermore, the work illustrates the significance of employing precession electron diffraction for mapping new materials landscapes resulting from tailored high-pressure and -temperature syntheses.

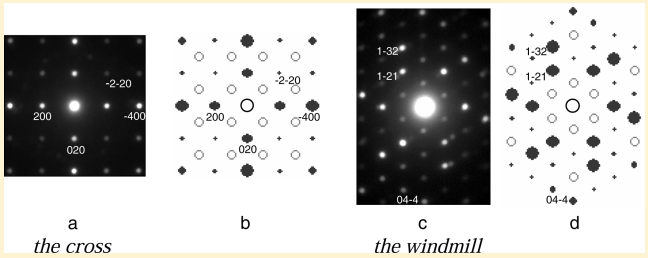

INTRODUCTION

While cubic diamond-structured silicon (Si) is the single most important material in the semiconductor industry, it has an indirect band gap[1] and a fixed lattice constant, constraining it from efficient light-emitting applications including, most prominently, photovoltaics and laser devices. This constraint remains present for its associated cubic diamond-structured pure germanium (Ge)[1] and Si−Ge alloy[2] counterparts because they also retain fundamental indirect band gaps. There is a strong drive, however, to extend the functionality of (Si, Ge)-based technology from microelectronics into optoelectronics. This has led to the investigation of a number of avenues, all based on processing of cubic diamond-structured Si or Ge, to address this constraint.[3,4] These avenues include doping Si with erbium (Er) to serve as a lasing center,[5] etching Si with hydrogen fluoride to create pores resulting in luminescence due to quantum confinement effects,[6] inducing tensile strain coupled with n-type doping in Ge to access direct-gap emission in the indirect-gap material,[7] and hybrid approaches[8] interfacing Si with other light-emitting chemical compounds.

Our approach is different. Rather than process the existing cubic diamond structure that does not intrinsically exhibit targeted properties, transform it instead to a different crystal symmetry that does. That is, develop a new $Si_{1-x}Ge_x$ material landscape by exploring the synthesis of new structures that intrinsically contain tunable properties including fundamental direct band gaps. To evaluate the optimal pressure and temperature regions for novel solid solution formation, we examine the phase relationships of the two end members, Si and Ge.[9,10] Si and Ge are both semiconductors with cubic diamond structure up to about 10 and 12 GPa, respectively.[11] Hence, synthesis within this pressure regime will only allow us to obtain the known cubic diamond-structured semiconducting SiGe equilibrium modification.[12] Above about 12 GPa, however, the end members are both metallic, having transformed to the β-tin (Sn) modification.[11,13] Ge retains this modification up to 75 GPa,[14,15] whereas Si undergoes several phase transitions: above 13 GPa,[16,17] it transforms to an orthorhombic phase, to a simple hexagonal phase above 15 GPa,[16,17] to another orthorhombic phase above 38 GPa,[18] and to a hexagonal close-packed phase above 42 GPa[19] (Figure 1). Hence, between 12 and 13 GPa, all four generally accepted criteria for solid solution formation, namely, the same crystal structure, atomic radii ratios within 15% of each other, and similar valencies and electronegativities, are fulfilled.[20]

This is not to say that at higher pressures synthesis of SiGe is not merited. While the crystal structures are indeed no longer the same, the atomic radii ratios are still within about 6% of each other and the electronic properties remain compatible (Figures 1 and 2). Furthermore, the melting points are virtually identical at 17 GPa, which serves as an additional barrier against

Received: February 20, 2014
Published: May 14, 2014

   dx.doi.org/10.1021/ic500416s | *Inorg. Chem.* 2014, 53, 5656−5662

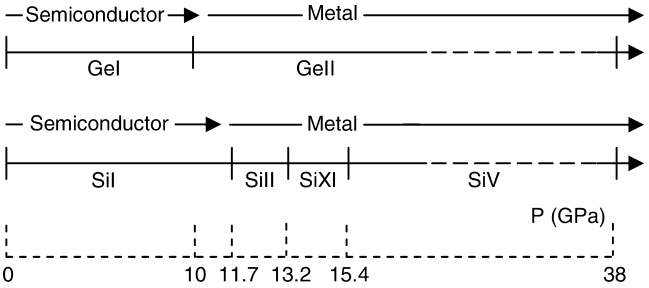

Figure 1. Comparison of the pressure-induced structural transitions of Ge and Si upon room temperature compression to 38 GPa. Semiconducting GeI (cubic diamond structure, $Fd\bar{3}m$) transforms to metallic GeII [β-Sn structure ($I4_1/amd$)] above 9 GPa. This structure is retained to 45 GPa. Semiconducting SiI (cubic diamond structure $Fd\bar{3}m$) transforms to metallic SiII [β-Sn structure ($I4_1/amd$)] above 11 GPa. Above 13 GPa, this phase transforms to an orthorhombic ($Imma$) modification, to a hexagonal modification (P_6/mmm) above 15 GPa, to another orthorhombic phase ($Cmca$) above 38 GPa, and to a further hexagonal modification ($P6_3/mmc$) above 42 GPa.

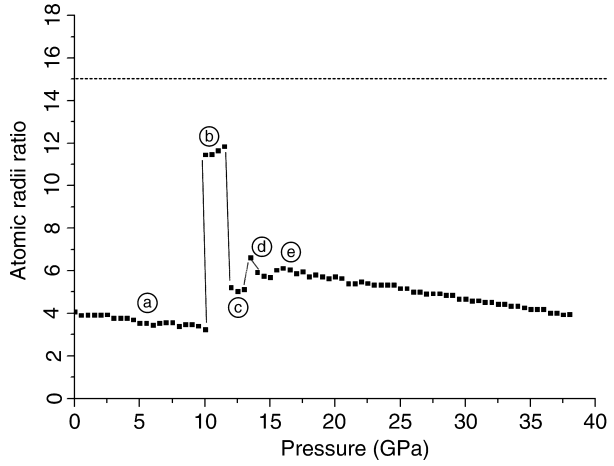

Figure 2. Ge−Si atomic radii ratio (% difference), pressure dependence from ambient to 38 GPa. Points a−e reveal respectively the ratios between GeI ($Fd\bar{3}m$) and SiI, GeII ($I4_1/amd$) and SiI ($Fd\bar{3}m$), GeII and SiII ($I4_1/amd$), GeII and SiXI ($Imma$), and GeII and SiV (P_6/mmm).[19,21−25] The dashed line depicts the Hume−Rothery tolerance atomic radius ratio boundary below which solid solution formation is favored.

segregation (Figure 3). In contrast,[29] at ambient pressure, despite the four criteria for solid solution being formally fulfilled, the more than 500 K melting point difference between Si and Ge leads, in actuality, to profound segregation effects. This makes extended homogeneous solid solution formation extremely difficult,[30] especially on the Ge-rich side, because of the larger segregation coefficients for Ge-rich compositions.[31,32] The impetus for synthesis and promise of obtaining technologically important, tunable novel solid solutions are reinforced by a host of recent experiments and calculations on the preparation, stability, and optoelectronic properties of Si and Ge phases.[33−42] Pure Ge obtained at ambient pressure from above 10−12 GPa is tetragonal ($P4_32_12$)[43] and is calculated to exhibit a direct band gap.[44]

Hence, a Ge-rich tetragonal GeSi solid solution should exhibit a tunable direct band gap.[45] Furthermore, Si with the $P4_32_12$ tetragonal modification could upon doping exhibit a higher superconducting temperature than those of the other Si modifications.[46] While Si does not form this tetragonal phase, a

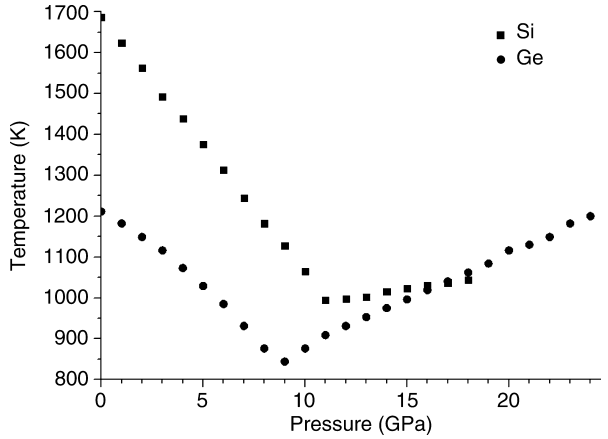

Figure 3. Pressure dependence of the melting points of Ge and Si.[9,26−28] The negative melting slopes for both elements are due to the higher density of their liquid states, which are metallic, unlike their solid states, which are semiconducting in the cubic diamond phase. Upon transition to metallic crystal structures at higher pressures, the melting slopes become positive. In the pressure regime of our experiments, the melting points of Ge and Si converge.

targeted solid solution with Ge, which does, could then lead to a bulk Si-based tetragonal phase with elevated superconducting T_c upon doping. Additionally, pure Si obtained at ambient conditions from above 12−13 GPa is cubic ($Ia\bar{3}$) and is a semimetal.[43,44] Thus, a Si solid solution with Ge within a complementary compositional range to that stabilizing a $P4_32_12$ phase can result in a compositionally tunable SiGe cubic ($Ia\bar{3}$) phase, which upon crystal size tuning may, because of multiple exciton generation and optimized band gap, be considered for solar conversion applications.[39] A disordered hexagonal phase (2H lonsdaleite)[47,48] for both Ge and Si has also been obtained at 1 atm from above 10 GPa for both Ge and Si. We perform, hence, here synthesis experiments at pressures between 12 and 17 GPa coupled with electron microscopy (EM) and synchrotron characterization experiments on a series of Ge and Si starting mixtures targeting new alloys in this system with tunable structure and properties.

EXPERIMENTAL SECTION

We employed ultrapure Ge pieces (99.9999+% puratronic Alfa Aesar) and Si pieces (99.999 metal basis % Alfa Aesar) as starting materials. The high-pressure experiments were performed at the German Research Centre for Geosciences in Potsdam. Seven multianvil experiments on Ge−Si mixtures placed in lidded aluminum oxide crucibles were performed: three at 12 GPa, two at 13 GPa, and two at 17 GPa. For the experiments at relatively low pressure (12 and 13 GPa), 14/8 assemblies (octahedral length/truncation length) were used, with a MgO-based octahedron serving as a pressure-transmitting medium. Details of the experimental setup are given in ref 49. The 17 GPa experiments were performed with a 10/5 assembly, which was calibrated using the following phase transitions: coesite−stishovite,[50] α−β-Mg_2SiO_4,[51] β−γ-Mg_2SiO_4,[52] and enstatite−β-Mg_2SiO_4−stishovite.[53] In all experiments, stepped graphite heaters were employed and temperatures were measured with type C thermocouples ($W_5Re/W_{26}Re$), with electromotive forces uncorrected for pressure.

At 12 GPa, 80:20, 50:50, and 20:80 atom % Ge−Si mixtures were melted at 1500 K for 2 min followed by annealing at 650 K for 1 h before temperature and then pressure quenching. At 13 GPa, 75:25 and 40:60 atom % Ge−Si mixtures were melted at 1500 K for 2 min followed by annealing at 650 K for 2 h before temperature and then pressure quenching. At 17 GPa, 75:25 and 60:40 atom % Ge−Si

dx.doi.org/10.1021/ic500416s | Inorg. Chem. 2014, 53, 5656−5662

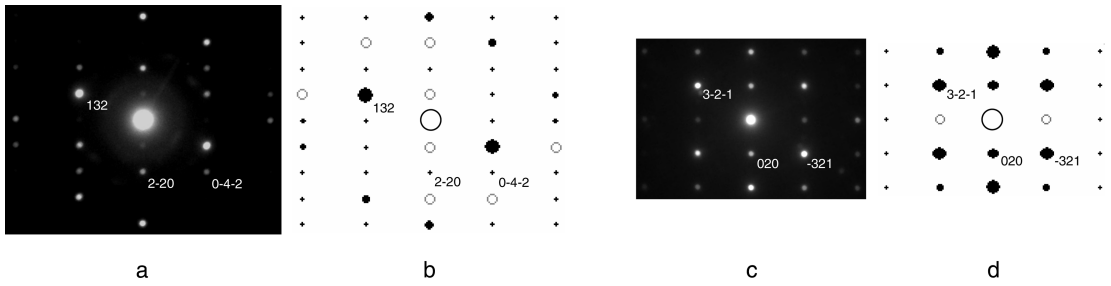

Figure 4. Experimental PED and simulated zone-axis diffraction patterns of binary Ge−Si crystals with the $Ia\bar{3}$ space group: (a and b) of the [11−2] zone axis; (c and d) of the [103] zone axis.

mixtures were melted at 1500 K for 2 min followed by annealing at 800 K for 2 h before temperature and then pressure quenching.

The samples were polished and carbon (C)-coated for EM measurements. Scanning electron microscopy (SEM; Philips XL30CP), with an energy-dispersive X-ray (EDX) analyzer (Oxford Instruments EDX detector; SiLi crystal with PGT spirit analysis software), was employed for chemical and morphological analysis from the polished pellets. The acceleration voltage used was set to 20 kV. Backscattered electron mode was primarily used because it allows for chemical contrast.[54,55] Samples were also investigated with a transmission electron microscopy (TEM) instrument (Philips CM30), equipped with a 1K × 1K Gatan slow-scan charge-coupled-device (CCD) camera and with *Digital Micrograph* software for the acquisition of electron diffraction patterns and bright-field imaging with an accelerating voltage of 300 kV. A double tilting stage allowed us to record multiple zone-axis patterns from single crystals. The CM30 instrument is also equipped with a Nanomegas "Spinning Star" precession system and a Noran EDX detector for local chemical analysis. The camera length for TEM was calibrated using pure Si. Semiquantitative chemical analysis was carried out without standards for determination of the Cliff−Lorimer factors and without measurement of the local thin-foil thickness. Precession electron diffraction (PED) measurements were performed in microdiffraction mode, i.e., with a nearly parallel incident beam focused on the specimen with a spot size in the range of 10−50 nm. The precession semiangle of 2° was set to record PED patterns. The maximum precession angle of about 3° was systematically used in order to further identify the kinematically forbidden reflections.[56−58] PED performed at a high precession semiangle of ≥2°, in particular, significantly reduces the overall dynamical effects involved in an electron diffraction pattern, which, in turn, allows for a drastically improved measurement of kinematical intensities of diffracted reflections from the single crystallites. This facilitates differentiation even between closely related diffraction patterns and concomitant accurate crystallographic indexing of the new phases.[56−63] Supporting angle-dispersive X-ray diffraction (XRD) measurements were performed at the ID11 beamline of the European Synchrotron Radiation Facility. A monochromatic X-ray beam (λ = 0.31849 Å) was focused to 10 μm × 7 μm using a tunable X-ray focusing apparatus (transfocator) containing 20 beryllium lenses and 254 aluminum lenses.[64] A Frelon 4M CCD detector was used for diffraction data collection with a pixel size of 50 × 50 μm^2. LaB_6 powder (National Institute of Standards SRM 660a), also placed in a square on a copper (Cu) grid and on kapton holders, was used to calibrate the distance and orientation of the detector. A Si fluorescence detector was also installed on ID11, which allowed us to obtain a chemical signature from the very spot from which diffraction was performed. The crystal sizes observed with EM ranged from about 50 nm to a few micrometers. The combination of PED/EM and XRD allows for highly spatially resolved structural and chemical analysis together with high angular resolution structural analysis. For characterization of small single crystals and/or a heterogeneous assembly, electron diffraction is particularly needed. For the electron diffraction and XRD measurements, particles of the reaction product from the polished half-capsules were taken under an 126× total magnification optical microscope, using a sharp tungsten carbide needle and dispersed onto the thin C film of labeled 3-mm-diameter Cu TEM grids (Agar scientific). For the XRD measurements, particles were placed on litholoops (Molecular Dimensions Limited) as well. For the litholoops, typically used for larger sample amounts, the principal advantage is the absence of any crystalline features (e.g., Cu in a grid) whose signal may interfere with the sample patterns. Thus, one can freely rotate the litholoop about its axis to obtain better powder averaging and minimize any texturing effects. On the basis of numerous comparative measurements, we found that the signal-to-noise ratio of the diffraction peaks of material placed on the TEM grid is typically about a factor of 2 higher than that from the litholoop. This may be attributed to the C foil of the TEM grid being more than 2 orders of magnitude thinner than the litholoop's rigid kapton foil (holes on the litholoop are typically too large for the small samples). Further beneficial attributes of the TEM grid are the greater ease in locating and aligning the sample with the beam because the sample is framed by the Cu grid and the better adherence of the material to the C foil. Equally, even with typically 45° rotation applied, the spatial resolution with a small beam spot sufficed in avoiding Cu diffraction peaks. Use of the TEM grid means that one can formally examine the same sample as that examined with TEM, which is particularly important for obtaining multifaceted complementary structural, chemical, and morphological information, particularly from precious material. The zone-axis electron diffraction patterns were interpreted using the software *Electron Diffraction*, version 7.01, by considering the kinematical approximation.[65] Note that in all of the simulated zone-axis diffraction patterns shown hereafter an empty circle represents a kinematically forbidden reflection and the size of a filled circle is proportional to the intensity of the diffracted reflection. The XRD patterns were circularly integrated using *Fit2D*,[66] and the one-dimensional patterns were fitted and indexed using the *Topas 3.0* software.[67] The chemical signatures taken from the samples at ID11 in-parallel with the diffraction were performed using the program *PyMCA*.[68]

■ RESULTS

PED analysis of numerous single crystallites with accompanying chemical analysis from each analyzed crystallite from the obtained products allowed us to develop a structure−composition map of the reaction products. We present examples documenting the $Ia\bar{3}$ assignment first, followed by examples documenting the $P4_32_12$ assignment and finally examples of our chemical analysis of crystals from both symmetries. Figure 4 shows representative zone-axis PED patterns of the Ge−Si crystallites obtained with $Ia\bar{3}$ symmetry (Figure 4a,c) together with their simulated diffraction patterns (Figure 4b,d), revealing the excellent match with the experimental data. A further Ge−Si experimental zone-axis PED pattern (Figure 5a) is compared with its corresponding simulated $Ia\bar{3}$ (Figure 5b) and its site-ordered $Pa\bar{3}$ symmetry analogue (Figure 5c), revealing that our new cubic binary Ge−Si phase exhibits no long-range site ordering. The importance of PED for unambiguous indexing of the $Ia\bar{3}$ space group is

dx.doi.org/10.1021/ic500416s | *Inorg. Chem.* 2014, 53, 5656−5662

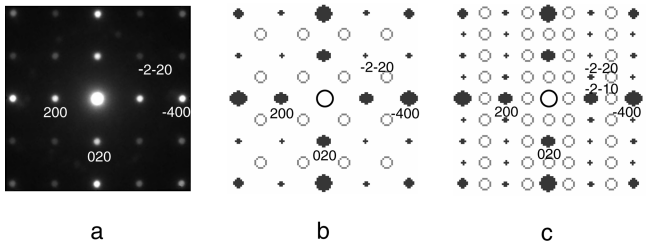

Figure 5. Comparison of an experimental zone-axis PED pattern of a binary Ge−Si crystal to simulated ones without ($Ia\bar{3}$) and with ($Pa\bar{3}$) site ordering. (a) Experimental PED [001] zone-axis pattern and simulated [001] zone axes with (b) $Ia\bar{3}$ and (c) $Pa\bar{3}$ space groups.

further illustrated in Figure 6 by comparing an experimental zone-axis diffraction pattern taken without (Figure 6a) and with

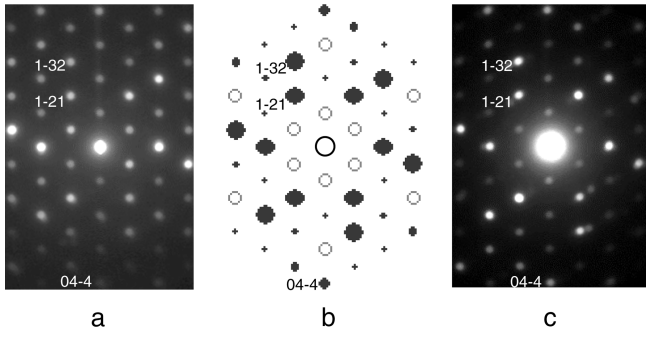

Figure 6. (a and c) Experimental [111] zone-axis electron diffraction pattern for a binary Ge−Si crystal with the $Ia\bar{3}$ space group measured without and with precession and a (b) simulated [111] zone-axis pattern.

(Figure 6c) precession to that of the corresponding simulated pattern (Figure 6b). Figure 7 shows representative zone-axis diffraction patterns of the Ge−Si crystallites obtained with $P4_32_12$ symmetry (Figure 7a,c) together with their simulated diffraction patterns (Figure 7b,d), revealing the excellent match with the experimental data. Unlike the cubic modification, consideration of a site-ordered analogue is not merited because it does not occur for the tetragonal phase.[69] The importance of PED for unambiguous indexing of the $P4_32_12$ space group is further illustrated in Figure 8 by comparing an experimental zone-axis diffraction pattern taken without (Figure 8a) and with (Figure 8c) precession to that of the corresponding simulated pattern (Figure 8b). The $Ia\bar{3}$ symmetry occurs for compositions from 100 atom % to about 23 atom % Si, with the $P4_32_12$ symmetry occurring for Si compositions from 22 atom % Si

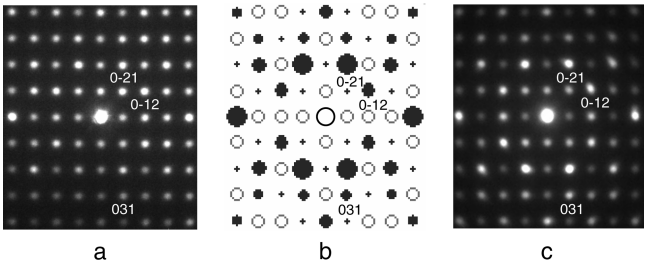

Figure 8. (a and c) Experimental [100] zone-axis electron diffraction pattern for a binary Ge−Si crystal with the $P4_32_12$ space group measured without and with precession and (b) a simulated [100] zone-axis pattern.

downward. Examples of chemical analysis taken from crystallites of both symmetries are shown in Figure 9a−c.

The only other highly crystalline symmetry detected from a few crystallites after release from 12 GPa was the ambient-pressure cubic diamond symmetry likely because this pressure may be close to the transition pressure between SiGe cubic diamond and the β-Sn modification.[70−75] Disordered structures with hexagonal symmetry, likely with varying polytypic characteristics, for a range of Ge−Si compositions were, however, also detected here from all pressures. These were more prevalent as the Ge content increased. Indeed, their enhanced presence in the reaction product matrix for Ge-richer compositions has hindered us so far from obtaining an accompanying XRD pattern of Ge−Si with $P4_32_12$ symmetry and will be the focus of a further report. Angle-dispersive XRD measurements, on the other hand, from binary $Ia\bar{3}$ Si-richer compositions were obtained. An XRD pattern from a sample extracted from a pellet, which has a bulk 20:80 Ge−Si composition based on chemical analysis using SEM, is shown in Figure 10.

DISCUSSION

We provide here an explanation for the composition−structure relationship measured and why, in particular, the binary Ge−Si cubic $Ia\bar{3}$ phase is obtained for a larger range of Ge−Si compositions than the $P4_32_12$ phase is. With respect to compression of Ge and Si (Figure 1), differences upon release from 17 GPa are that GeII transforms to $P4_32_12$ below about 9 GPa and is retained at 1 atm, and SiII transforms to an $R\bar{3}$ phase below about 9 GPa before $Ia\bar{3}$ is obtained below 2 GPa and retained at 1 atm.[10,43] The Si $Ia\bar{3}$ and Ge $P4_32_12$ phases are stable indefinitely at ambient conditions.

These crystal structures, rather than the cubic diamond structure, are obtained because they are kinetically accessible from denser phases upon release.[76] Indeed, even intermediate

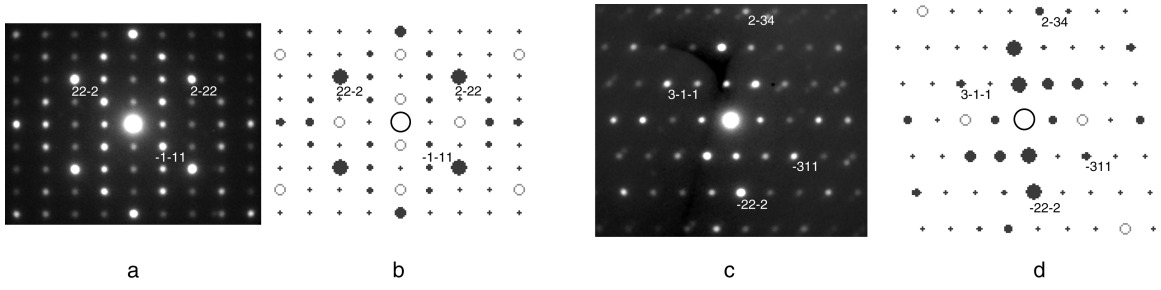

Figure 7. Experimental PED and simulated zone-axis diffraction patterns of binary Ge−Si crystals with the $P4_32_12$ space group: (a and b) of the [011] zone axis; (c and d) of the [121] zone axis.

dx.doi.org/10.1021/ic500416s | Inorg. Chem. 2014, 53, 5656−5662

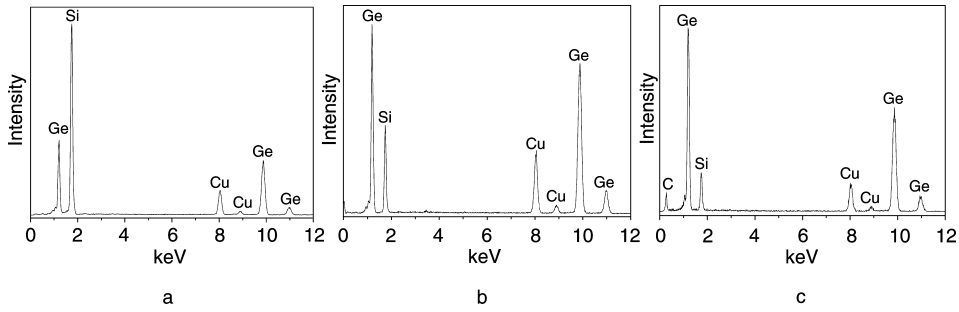

Figure 9. Examples of TEM/EDX chemical analysis from Ge−Si crystals obtained at ambient conditions after high-pressure and temperature syntheses. (a and b) Semiquantitative EDX analysis from two crystals with the $Ia\bar{3}$ space group revealing $Ge_{0.25}Si_{0.75}$ and $Ge_{0.65}Si_{0.35}$ stoichiometries, respectively, and one (c) with the $P4_32_12$ space group, revealing a $Ge_{0.81}Si_{0.19}$ stoichiometry. The C and Cu peaks originate respectively from the C foil and Cu grid of the TEM sample holder.

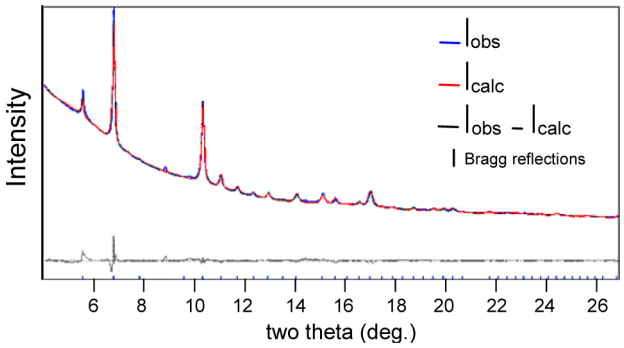

Figure 10. XRD pattern of a $Ge_{0.2}Si_{0.8}$ composition with the $Ia\bar{3}$ space group [a = 6.676 (1) Å] and a calculated density of ρ = 3.303 g/cm^3. We have, to date, also measured the XRD pattern of a $Ge_{0.5}Si_{0.5}$ composition with the $Ia\bar{3}$ space group [a = 6.782 (1) Å] and a calculated density of ρ = 4.287 g/cm^3. For reference, the corresponding densities of cubic diamond $Fd\bar{3}m$ $Ge_{0.2}Si_{0.8}$ and $Ge_{0.5}Si_{0.5}$ are respectively ρ = 2.998 and 3.938 g/cm^3.[12]

heating experiments on Si $Ia\bar{3}$ result in a hexagonal ($P6_3mc$ 2H) rather than the diamond phase because the bond reconstruction required for the latter is too severe.[43,47] The internal energies of the $P4_32_12$ and $Ia\bar{3}$ phases are very similar.[44,77] Why Ge favors $P4_32_12$ while Si favors the $Ia\bar{3}$ phase can be explained from a structural point of view.[44,69] Ge $P4_32_12$ and Si $Ia\bar{3}$ are composed of tetrahedral units, as is their lowest-energy, but kinetically inaccessible cubic diamond $Fd\bar{3}m$ counterpart. In Ge and Si $Fd\bar{3}m$, the tetrahedra are undistorted and characterized by a single bond length. Deviation from this structure by $P4_32_12$ and $Ia\bar{3}$ has two energetic penalties: (1) the degree of tetrahedral bond angle distortion and (2) the degree of deviation from the diamond $Fd\bar{3}m$ bond length. $P4_32_12$ allows for a greater proximity of its bond lengths to that of $Fd\bar{3}m$ at the cost of greater tetrahedral bond angle distortions. Conversely, $Ia\bar{3}$ allows for smaller tetrahedral bond angle distortions at the cost of greater deviation of the bond lengths from those in the $Fd\bar{3}m$ diamond phase.[77] Ge adopts the $P4_32_12$ structure because the Ge bonds are less stiff than those of Si (vibrational frequencies are lower than those in Si). Hence, its structure can accommodate greater angular distortions with relative ease, benefiting, on the other hand, from bond lengths closer to those of the $Fd\bar{3}m$ diamond. The Si bonds, on the other hand, are stiff, requiring the structure to remain relatively undistorted, at the expense, however, of a greater distribution of bond lengths with respect to those in the $Fd\bar{3}m$ diamond. Despite their very similar energies, the $Ia\bar{3}$ symmetry may be viewed as slightly favored based on the additional observation that the $P4_32_12$ symmetry is not accessible for end member Si, whereas the $Ia\bar{3}$ symmetry can be accessed by Ge under rapid pressure release, albeit fleetingly, with ensuing transition to a hexagonal ($P6_3mc$ 2H) phase.[78]

Another reason that the $Ia\bar{3}$ symmetry may be compositionally more favored, even for same group members, is because of an energetic cost to having same element nearest neighbors.[10,69] While group IV binaries with $P4_32_12$[79] and $Ia\bar{3}$ symmetries (Figure 5) both adopt structures without long-range site ordering, only the $Ia\bar{3}$ symmetry has an equivalent site-ordered $Pa\bar{3}$ description,[80] which allows nearest neighbors to be of the second element. $P4_32_12$ does not have this option because, unlike $Ia\bar{3}$, it contains rings with odd numbers of atoms.[10,69,81] Hence, local level site ordering[10] to alleviate any residual strain is only favored for the $Ia\bar{3}$ symmetry. These considerations provide an explanation for why, within this newly established SiGe materials landscape, the $Ia\bar{3}$ symmetry spans a wider range of compositions than the $P4_32_12$ symmetry does.

CONCLUSIONS

The combination of high pressures and temperatures has allowed us to form a materials landscape for Ge_xSi_{1-x} $0 < x < 1$ containing tetragonal $P4_32_12$ and cubic $Ia\bar{3}$ symmetries, with projected electronic character ranging from semiconducting to semimetallic, of optoelectronic, transport, and thermoelectric interest.[39,46] Further, Ge−Si alloying, in addition to providing tunability of the properties, can also contribute to greater structural stability. For example, Ge alloys with tetragonal symmetry exhibit enhanced cycling performance as battery anodes.[40] The work here also includes the first participation of Si in a $P4_32_12$ alloy and, together with the new phase relationships in Ge−Sn,[79,82,83] paves the way for even greater tunability in novel ternary Si−Ge−Sn systems. The work also reveals the effectiveness of linking, together with X-rays, PED with extreme conditions for creation, and characterization of new materials landscapes. This highest possible spatially resolved detection of new single crystallites and their distinct structural analysis based on both spot positional distribution and a kinematical intensity profile markedly limits ambiguity of the assignment and facilitates confident advance.

AUTHOR INFORMATION

Corresponding Author

*E-mail: george.serghiou@ed.ac.uk.

dx.doi.org/10.1021/ic500416s | Inorg. Chem. 2014, 53, 5656−5662

Present Address

[#]P.J.: Safetec UK Limited, 16 Albert Street, Aberdeen AB25 1XQ, U.K.

Notes

The authors declare no competing financial interest.

■ ACKNOWLEDGMENTS

We are grateful to Professor Jean-Paul Morniroli for his guidance and support. The TEM facility in Lille (France) is supported by the Conseil Regional du Nord-Pas de Calais and the European Regional Development Fund. We also acknowledge EU proposal MA712 for experiments at the European Radiation Synchrotron Facility. We also thank the Moray Foundation and the Innovative Initiative grant program for support. We further warmly thank Ahmed Addad for his work and consultation on chemical microanalysis using TEM, Nicola Cayzer for consultation on SEM, Michael Hall for demanding solids processing, and Mark Gibbard for some data processing. We also thank Reiner Schulz and Andreas Ebert for their support during the multianvil experiments.

■ REFERENCES

(1) Hybertsen, M. S.; Louie, S. G. *Phys. Rev. B* **1986**, *34*, 5390−5413.
(2) Braunstein, R.; Moore, A. R.; Herman, F. *Phys. Rev. B* **1958**, *109*, 695−710.
(3) Cloutier, S. G.; Kossyrev, P. A.; Xu, J. *Nat. Mater.* **2005**, *4*, 887−891.
(4) Kuo, Y. H.; Lee, Y. K.; Ge, Y. S.; Ren, S.; Roth, J. E.; Kamins, T. I.; Miller, D. A. B.; Harris, J. S. *Nature* **2005**, *437*, 1334−1336.
(5) Vinh, N. Q.; Ha, N. N.; Gregorkiewicz, T. *Proc. IEEE* **2009**, *97*, 1269−1283.
(6) Adachi, S.; Oi, M. *J. Appl. Phys.* **2007**, *102*, 063506−063515.
(7) Liu, J.; Sun, X.; Pan, D.; Wang, X.; Kimerling, L. C.; Koch, T. L.; Michel, J. *Opt. Expr.* **2007**, *15*, 11272−11277.
(8) Vasdekis, A. E.; Moore, S. A.; Ruseckas, A.; Krauss, T. F.; Samuel, I. D. W.; Turnbull, G. A. *Appl. Phys. Lett.* **2007**, *91*, 051124−051127.
(9) Young, D. A. *Phase Diagrams of the Elements*, 1st ed.; University of California Press: Berkeley, CA, 1991.
(10) Mujica, A.; Rubio, A.; Munoz, A.; Needs, R. J. *Rev. Mod. Phys.* **2003**, *75*, 863−912.
(11) Bundy, F. P. *J. Chem. Phys.* **1964**, *41*, 3809−3814.
(12) Dismukes, J. P.; Paff, R. J.; Ekstrom, L. *J. Phys. Chem.* **1964**, *68*, 3021−3027.
(13) Jamieson, J. C. *Science* **1963**, *139*, 762−764.
(14) Vohra, Y. K.; Brister, K. E.; Desrgeniers, S.; Ruoff, A. L.; Chang, K. J.; Cohen, M. L. *Phys. Rev. Lett.* **1986**, *56*, 1944−1947.
(15) Nelmes, R. J.; Liu, H.; Belmonte, S. A.; Loveday, J. S.; McMahon, M. I.; Allan, D. R.; Hausermann, D.; Hanfland, M. *Phys. Rev. B* **1996**, *53*, R2907−R2909.
(16) McMahon, M. I.; Nelmes, R. J.; Wright, N. G.; Allan, D. R. *Phys. Rev. B* **1994**, *50*, 739−743.
(17) Lewis, S. P.; Cohen, M. L. *Phys. Rev. B* **1993**, *48*, 16144−16147.
(18) Hanfland, M.; Schwarz, U.; Syassen, K.; Takemura, K. *Phys. Rev. Lett.* **1999**, *82*, 1197−1200.
(19) Hu, J. Z.; Merkle, L. D.; Menoni, C. S.; Spain, I. L. *Phys. Rev. B* **1986**, *34*, 4679−4684.
(20) Hume-Rothery, W.; Smallman, R. E.; Haworth, C. W. *The Structure of Metals and Alloys*, 5th ed.; The Chaucer Press: London, 1969.
(21) Chang, K. J.; Cohen, M. L. *Phys. Rev. B* **1986**, *34*, 8581−8590.
(22) Di Cicco, A.; Frasini, A. C.; Minicucci, M.; Principi, E.; Itie, J. P.; Munsch, P. *Phys. Status Solidi B* **2003**, *240*, 19−28.
(23) Mcskimin, H. J.; Andreatch, P. *J. Appl. Phys.* **1964**, *35*, 2161−2165.
(24) McMahon, M. I.; Nelmes, R. J.; Wright, N. G.; Allan, D. R. *Phys. Rev. B* **1994**, *50*, 739−743.
(25) Gaal-Nagy, K.; Strauch, D. *Comput. Mater. Sci.* **2004**, *30*, 8−15.
(26) Prakapenka, V.; Kubo, A.; Kuznetsov, A.; Laskin, A.; Shkurikhin, O.; Dera, P.; Rivers, M. L.; Sutton, S. R. *High Pressure Res.* **2008**, *28*, 225−235.
(27) Kubo, A.; Wang, Y.; Runge, C. E.; Uchida, T.; Kiefer, B.; Nishiyama, N.; Duffy, T. S. *J. Phys. Chem. Solids* **2008**, *69*, 2255−2260.
(28) Voronin, G. A.; Pantea, C.; Zerda, T. W.; Zhang, J.; Wang, L.; Zhao, Y. *J. Phys. Chem. Solids* **2005**, *64*, 2113−2119.
(29) Serghiou, G.; Odling, N.; Hunter, R.; Abbie, A.; Armstrong, B.; Lathe, C. *High Pressure Res.* **2014**.
(30) Schilz, J.; Romanenko, V. N. *J. Mater. Sci.: Mater. Electron.* **1995**, *6*, 265−279.
(31) Dario, A.; Sicim, A. O.; Balicki, E. *J. Cryst. Growth* **2011**, *337*, 65−71.
(32) Kostylev, I.; Woodacre, J. K.; Lee, Y. P.; Klages, P.; Labrie, D. *J. Cryst. Growth* **2013**, *377*, 147−152.
(33) Zhang, P. H.; Crespi, V. H.; Chang, E.; Louie, S. G.; Cohen, M. L. *Nature* **2001**, *409*, 69−71.
(34) Botti, S.; Flores-Livas, J. A.; Amsler, M.; Goedecker, S.; Marques, M. A. L. *Phys. Rev. B* **2012**, *86*, 121204−121209.
(35) Malone, B. D.; Louie, S. G.; Cohen, M. L. *Phys. Rev. B* **2010**, *81*, 115201−115206.
(36) Kim, S. J.; Quy, O. K.; Chang, L.-S.; Stach, E. A.; Handwerker, C. A.; Wei, A. *J. Mater. Chem.* **2010**, *20*, 331−337.
(37) Sato, S.; Nozaki, S.; Morisaki, H. *Appl. Phys. Lett.* **1998**, *72*, 2460−2462.
(38) Selli, D.; Boulfelfel, S. E.; Baburin, I. A.; Seifert, G.; Leoni, S. *RSC Adv.* **2012**, *2*, 8833−8839.
(39) Wippermann, S.; Voeroes, M.; Rocca, D.; Gali, A.; Zimanyi, G.; Galli, G. *Phys. Rev. Lett.* **2013**, *110*, 046804−046809.
(40) Cho, Y. J.; Im, H. S.; Kim, H. S.; Myung, Y.; Back, S. H.; Lim, Y. R.; Jung, C. S.; Jang, D. M.; Park, J.; Cha, E. H.; Il Cho, W.; Shojaei, F.; Kang, H. S. *ACS Nano* **2013**, *7*, 9075−9084.
(41) Johnson, B. C.; Haberl, B.; Deshmukh, S.; Malone, B. D.; Cohen, M. L.; McCallum, J. C.; Williams, J. S.; Bradby, J. E. *Phys. Rev. Lett.* **2013**, *110*, 085502−085507.
(42) Xiang, H. J.; Huang, B.; Kan, E.; Wei, S. H.; Gong, X. G. *Phys. Rev. Lett.* **2013**, *110*, 118702−118706.
(43) Kasper, J. S.; Richards, S. M. *Acta Crystallogr.* **1964**, *17*, 752−755.
(44) Mujica, A.; Needs, R. J. *Phys. Rev. B* **1993**, *48*, 17010−17017.
(45) Bottomley, D. J.; Delaunay, J. J.; Tomita, M.; Hayashi, T. *Thin Solid Films* **2002**, *402*, 143−153.
(46) Malone, B. D.; Sau, J. D.; Cohen, M. L. *Phys. Rev. B* **2008**, *78*, 035210−035217.
(47) Wentorf, R. H.; Kasper, J. S. *Science* **1963**, *139*, 338−339.
(48) Minomura, S. *J. Phys., Colloq.* **1981**, *42*, 181−188.
(49) Koch-Müller, M.; Rhede, D.; Schulz, R.; Wirth, R. *Phys. Chem. Miner.* **2009**, *36*, 329−341.
(50) Akaogi, M.; Yusa, H.; Shiraishi, K.; Suzuki, T. *J. Geophys. Res.* **1995**, *100*, 337−347.
(51) Morishima, H.; Kato, T.; Suto, M.; Ohtani, E.; Urakawa, S.; Utsumi, W.; Shimomura, O.; Kikegawa, T. *Science* **1994**, *26*, 1202−1203.
(52) Inoue, T.; Irifune, T.; Higo, Y.; Sanehira, T.; Sueda, Y.; Yamada, A.; Shinmei, T.; Yamazaki, D.; Ando, J.; Funakoshi, K.; Utsumi, W. *Phys. Chem. Miner.* **2006**, *33*, 106−114.
(53) Gasparik, T. *Contrib. Mineral. Petrol.* **1989**, *102*, 389−405.
(54) Goldstein, J. I.; Newbury, D. E.; Echlin, P. *Scanning Electron Microscopy and X-ray Microanalysis*; Plenum Press: New York, 1992.
(55) McGaff, A. J.; Serghiou, G.; Frost, D. J. *High Pressure Res.* **2008**, *28*, 491−495.
(56) Vincent, R.; Midgley, P. A. *Ultramicroscopy* **1994**, *53*, 271−282.
(57) Morniroli, J. P.; Auchterlonie, G. J.; Drennan, J.; Zou, J. *J. Microsc.* **2008**, *232*, 7−26.
(58) Morniroli, J. P.; Ji, G. *Mater. Res. Soc. Symp. Proc.* **2009**, *1184*, 37−48.
(59) Ji, G.; Morniroli, J. P.; Aucherlonie, G. J.; Drnnan, J.; Jacob, D. *Ultramicroscopy* **2009**, *109*, 1282−1294.

(60) Morniroli, J. P.; Ji, G.; Jacob, D. *Ultramicroscopy* **2012**, *121*, 42−60.
(61) Jacob, D.; Ji, G.; Morniroli, J. P. *Ultramicroscopy* **2012**, *121*, 61−71.
(62) Ji, G.; Morniroli, J. P. *J. Appl. Crystallogr.* **2013**, *46*, 430−442.
(63) Hadermann, J.; Abakumov, A. M.; Turner, S.; Hafideddine, Z.; Khasanova, N. R.; Antipov, E. V.; Van Tendeloo, G. *Chem. Mater.* **2011**, *23*, 3540−3545.
(64) Vaughan, G. B. M.; Wright, J. P.; Bytchkov, A.; Rossat, H.; Gleyzolle, I.; Snigireva, I.; Snigirev, A. *J. Synchrotron Radiat.* **2011**, *30*, 125−133.
(65) Morniroli, J. P. *Electron Diffraction* version 7.01; LMPGM UMR CNRS 8517: Lille, France, 2004.
(66) Hammersley, A. P.; Svensson, S. O.; Hanfland, M.; Fitch, A. N.; Hausermann, D. *High Pressure Res.* **1996**, *14*, 235−248.
(67) *TOPAS*; Bruker AXS: Karlsruhe, Germany, 2006.
(68) Solé, V. A.; Papillon, E.; Cotte, M.; Walter, Ph.; Susini, J. *Spectrochim. Acta, Part B* **2007**, *62*, 63−68.
(69) Crain, J.; Ackland, G. J.; Clark, S. J. *Rep. Prog. Phys.* **1995**, *58*, 705−754.
(70) Queisser, G.; Grosshans, W. A.; Holzapfel, W. B. *Europhys. Lett.* **1987**, *3*, 1109−1112.
(71) Lv, M. Y.; Chen, Z. W.; Liu, R. P.; Wang, W. K. *Solid State Commun.* **2005**, *135*, 749−752.
(72) Werner, A.; Sanjuro, J. A.; Cardona, M. *Solid State Commun.* **1982**, *44*, 155−158.
(73) Soma, T.; Iwanami, H.; Matsuo, H. *Solid State Commun.* **1982**, *42*, 469−471.
(74) da Silva, C. R. S.; Venezuela, P.; da Silva, A. J. R.; Fazzio, A. *Solid State Commun.* **2001**, *120*, 369−373.
(75) Hao, A.; Zhang, L.; Gao, Z.; Zhu, Y.; Liu, R. P. *Phys. Status Solidi B* **2011**, *248*, 1135−1138.
(76) Wang, J.-T.; Chen, C.; Mizuseki, H.; Kawazoe, Y. *Phys. Rev. Lett.* **2013**, *110*, 165503−166508.
(77) Clark, S. J.; Ackland, G. J.; Crain, J. *Phys. Rev. B* **1994**, *49*, 5341−5352.
(78) Nelmes, R. J.; McMahon, M. I.; Wright, N. G.; Allan, D. R.; Loveday, J. S. *Phys. Rev. B* **1993**, *48*, 9883−9886.
(79) Guillaume, C.; Serghiou, G.; Thomson, A.; Morniroli, J. P.; Frost, D. J.; Odling, N.; Mezouar, M. *J. Am. Chem. Soc.* **2009**, *131*, 7550−7551.
(80) Hull, S.; Keen, D. A. *Phys. Rev. B* **1994**, *50*, 5868−5885.
(81) Lambrecht, W. R. L.; Amador, C.; Segall, B. *Phys. Rev. Lett.* **1992**, *68*, 1363−1366.
(82) Guillaume, C. L.; Serghiou, G.; Thomson, A.; Morniroli, J. P.; Frost, D. J.; Odling, N.; Jeffree, C. E. *Inorg. Chem.* **2010**, *49*, 8230−8236.
(83) Serghiou, G.; Guillaume, C. L.; Jeffree, C. E.; Thomson, A.; Frost, D. J.; Morniroli, J. P.; Odling, N. *High Pressure Res.* **2010**, *30*, 44−50.